PHYSICAL REVIEW D VOLUME 34, NUMBER 9 1 NOVEMBER 1986

Inclusive hadronic production cross sections measured in proton-nucleus collisions at $\sqrt{s} = 27.4$ GeV

J. A. Crittenden,[a] Y. B. Hsiung,[b] and D. M. Kaplan[c]
Columbia University, New York, New York 10027

J. R. Hubbard, Ph. Mangeot, and A. Peisert[d]
Centre d'Etudes Nucléaires de Saclay, 91191 Gif-sur-Yvette, France

G. Charpak and F. Sauli
CERN, Geneva, Switzerland

C. N. Brown, S. Childress, D. A. Finley, A. S. Ito, A. M. Jonckheere, H. Jostlein,
L. M. Lederman, R. Orava,[e] S. R. Smith,[f] K. Sugano,[g] and K. Ueno[h]
Fermi National Accelerator Laboratory, Batavia, Illinois 60510

A. Maki
KEK, Ibaraki-ken, 305 Japan

Y. Sakai,[i] Y. Hemmi, K. Miyake, and T. Nakamura
Kyoto University, Kyoto, 606 Japan

M. R. Adams,[j] H. D. Glass,[k] D. E. Jaffe, J. Kirz, and R. L. McCarthy
State University of New York at Stony Brook, Stony Brook, New York 11794

R. Gray, R. E. Plaag, J. E. Rothberg, J. P. Rutherfoord, and K. K. Young
University of Washington, Seattle, Washington 98195

(Received 24 February 1986)

We present results on the production of hadrons in collisions of 400-GeV/c protons with beryllium, copper, and tungsten nuclei. The data cover the region from 5.6 to 8.0 GeV/c in the transverse momentum of the final-state hadron and from 73° to 102° in the proton-nucleon center-of-momentum frame production angle θ^*. The restriction of the data to values of x_T ($x_T = 2p_T/\sqrt{s}$) greater than 0.4 enriches the sample with hard collisions of valence quarks. Asymmetries about $\theta^* = 90°$ reflect the presence of neutrons in the target nuclei. The variation of the atomic-weight dependence parameter α with production angle is discussed in the context of the phenomenology of nucleonic structure within nuclei. We also extrapolate our measurements to a "deuteron" target to minimize nuclear effects and compare the result to QCD calculations.

I. INTRODUCTION

During the past ten years measurements of the transverse-momentum (p_T) spectra of hadrons produced in hadronic interactions have proven useful in understanding these processes in terms of quantum chromodynamical (QCD) models. Experiments[1] performed at the Fermi National Accelerator Laboratory (Fermilab) indicated a steep dependence on p_T of the invariant production cross section $E\,d^3\sigma/dp^3$ ($\sim p_T{}^{-8}$). This dependence was shown to be consistent with the effects of scaling violations in the distribution and fragmentation functions and the dependence of the strong coupling constant α_s on momentum transfer if the constituents in the colliding hadrons are assumed to have a Gaussian intrinsic-transverse-momentum (k_T) distribution with an average value $\langle k_T \rangle = 850$ MeV/c (Ref. 2). Later, experiments[3] performed in the Intersecting Storage Rings (ISR) at CERN showed that the p_T dependence flattens out at values of p_T greater than 10 GeV/c as predicted by the QCD models. These experiments demonstrated that a final-state hadron produced at high transverse momentum carries a large fraction (> 80%) of the momentum of its parent constituent. The consistency of the QCD models with both the Fermilab and CERN experiments was particularly impressive since the Fermilab measurements were made at significantly higher values of the scaling variable $x_T = 2p_T/\sqrt{s}$. This implied that a much larger fraction of the constituent interactions observed involved valence quarks, while the CERN measurements were made in a kinematic region favored by the interactions of gluons and sea quarks. The ability of the models to provide a consistent explanation of both measurements stimulated confidence in the QCD approach.

The experiments performed at Fermilab described above also measured an unexpected dependence of the invariant cross section on the atomic weight (A) of nuclear targets. The invariant cross section was found to scale with a power of A as expected, but for hadrons with transverse momenta above 2 GeV/c, the power (α) was measured to be significantly greater than 1.0. This apparently collective interaction was surprising in view of the large momentum transfers implied by the high transverse momenta of the final-state hadrons. Extensive work has been done on models[4] which hypothesize multiple scatters, within the nucleus, of the parton which is eventually dressed to form the observed final-state hadron. It is generally assumed that the formation of the hadron occurs outside the nucleus. (Recent experimental evidence supports this hypotheses for nuclei as heavy as copper.[5]) Since in most cases one of the scatters is of relatively low momentum transfer, perturbative QCD calculations are excluded and these models remain disturbingly phenomenological. In 1983 measurements of muon inelastic scattering from nuclear targets at CERN (Ref. 6) demonstrated an atomic-weight dependence of the inelastic structure functions of nucleons. An experiment performed at the Stanford Linear Accelerator[7] (SLAC) extended the measurements to a large number of nuclear species for deeply inelastic electron scattering as well. The ensuing flurry of theoretical interpretations included the suggestion that quarks are more loosely bound in nuclear matter than in free nucleons[8] and the consideration of more conventional nuclear effects involving interactions with the pion clouds surrounding nucleons in nuclei.[9] The magnitude of the effect (10–20% differences between the nucleon structure function in deuterium and that in a nucleus as heavy as tungsten) is slight compared to that observed in the production of hadrons with high transverse momenta. Its effect on the latter process has been calculated[10] and produces a slight decrease in the expected value of α for transverse momenta above 4 GeV/c.

These are the issues to be addressed by the measurements presented here. The data to be discussed were taken during the first run of experiment 605 at Fermilab. The experimental arrangement for that data run is described in Sec. II. Details of the data acquisition are presented in Sec. III. Section IV deals with the data analysis techniques and Sec. V presents the physical measurements and a discussion of these results.

II. THE EXPERIMENTAL TECHNIQUE AND THE APPARATUS

A. General

The E605 apparatus[11] was designed to detect single charged particles produced with high transverse momenta and pairs of oppositely charged particles produced with high invariant masses. A schematic diagram of the apparatus is shown in Fig. 1, as is the standard coordinate system. About 10% of the 5×10^9 incident protons per second interacted in the metal target located 10 cm upstream of the first dipole analyzing magnet (SM12). A forward beam dump within SM12 and the large vertical transverse momentum kick of SM12 (5.5 GeV/c) allowed an instantaneous luminosity per nucleon of 3×10^{34} cm^{-2}s^{-1}. This luminosity was limited by background singles rates in the spectrometer downstream of SM12. The SM12/dump configuration permitted no neutral particles to enter the downstream spectrometer directly from the target. The chosen geometry allowed charged particles of transverse momenta between 4 and 9 GeV/c to traverse the open aperture of the SM12 magnet, the particles of positive charge passing above the beam dump and those of negative charge below. Because of a 3.4-mrad vertical tilt of the incident beam the acceptance for positively charged particles differed from that for negatively charged particles. Accepted positive particles were produced with center-of-momentum frame production angles θ^* between 70° and 125°, while accepted negative particles were limited to production angles between 80° and 120°.

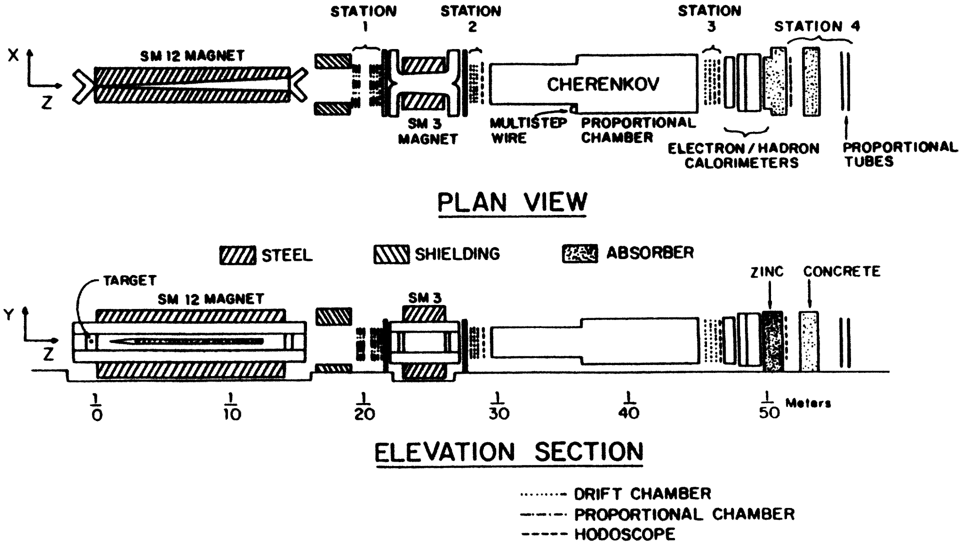

FIG. 1. A schematic diagram of the E605 apparatus.

(The calorimeter trigger requirement further reduced the angular range of the recorded data, as described in Sec. III.) The spectrometer afforded measurement resolutions of 0.2% in momentum, 0.5% in transverse momentum, and 0.3% in production angle. The resolution in these variables was determined primarily by the angular divergence in the incident beam and the multiple scattering of the final-state hadron in the target material.

B. Beam and targets

Experiment 605 used a Meson Laboratory beam ($M1$), which was produced by diffractive scattering of the primary beam arriving at the Meson Lab from the main ring of the accelerator. The beam arrived in 2-ns bursts (referred to as bunches) 18.9 ns apart during a period of 1 s (called a spill) every 10 s. During this first run of the experiment the beam had an X angle of 11 mrad and a Y angle of 3.4 mrad with respect to the spectrometer Z axis. At the target the beam had an angular divergence of 0.15 ± 0.05 mrad (rms) in the X dimension and of 0.25 ± 0.05 mrad (rms) in the Y dimension. The divergence in the Y dimension contributed significantly to the measurement resolution in transverse momentum and in production angle. The beam was measured to be 0.40 ± 0.1 mm (rms) wide in the Y dimension and 5.0 ± 1.5 mm wide in the x dimension.

A target monitor constructed as a scintillation-counter telescope viewed the target at a lab angle of 90°. The rate in this counter ($\sim$400 Hz) was recorded each spill and served to measure the number of protons interacting in the target. It was calibrated by comparing its counting rate to the activation of aluminum and copper foils placed in the incident beam during a dedicated run on the beryllium target. The copper and tungsten target data were normalized with respect to the beryllium target data by comparing the target monitor rate for each target to the rate in a secondary emission monitor (SEM) which measured the beam flux upstream of the target. This comparison of the target monitor rate for different targets was repeated each time the target was changed, at intervals of approximately two hours.

Table I shows the dimensions of the beryllium, copper, and tungsten targets. By scanning the target through the beam in increments of the target width, the fraction of the beam passing through the target was determined periodically throughout the run. Typical measurements yielded targeting of 70%, consistent with the transverse size of the beam expected from the beam transport emulation programs and the measurements of beam size mentioned above. About 10% of the incident beam particles suffered inelastic nuclear collisions in the targets, so the interaction rate was about 10 interactions per bunch, or 500 MHz. Table II lists the total integrated luminosities obtained on each target. For the purposes of calculating cross sections we used an effective integrated luminosity which accounted for attenuation of the incident beam in the target. The attenuation factors were 0.87, 0.91, and 0.91 for the beryllium, copper, and tungsten targets, respectively. Contamination of the data sample due to secondary interactions in the target was estimated to be negligible compared to the roughly 10% statistical uncertainties in the measurements of cross sections.

TABLE I. Parameters of the targets.

	Be	Cu	W
Horizontal width (mm)	38.3	38.1	38.1
Vertical thickness (mm)	0.996	0.914	1.059
Length (mm)	101.8	25.8	13.1
Nuclear weight A	9.01	63.54	183.85
Density (g/cm^3)	1.848	8.96	19.3
Number of nucleons per unit area (10^{25} cm^{-2})	1.13	1.39	1.52

C. Magnets

The SM12 and SM3 magnet yokes were built with 2000 tons of steel from the Nevis Laboratories cyclotron magnet. The SM12 magnet was 14.6 m long. It was tapered in the X dimension to accommodate all particles produced with an X angle of less than 34 mrad with respect to the spectrometer axis, reaching an open aperture of 0.9×1.2 m^2 at its downstream end. The resulting magnetic field shape is shown in Fig. 2. The field was oriented in the X direction, deflecting charged particles in the vertical plane. The chosen operating current was 2000 A, about half of maximum excitation, and the resulting transverse momentum kick was 5.5 GeV/c.

The SM3 aperture measured 1.3×1.7 m^2 over its 3.2 m length, with a slight taper in its X dimension. It was operated at a current of 3200 A, roughly three-quarters of full excitation. The magnetic field was oriented in the same direction as that of the SM12 magnet. Its shape is shown in Fig. 2. The total transverse-momentum kick was 0.72 GeV/c.

TABLE II. Integrated luminosities per nucleon on each target.

Target	Protons on target	Integrated luminosity per nucleon (cm^{-2})
Beryllium	$(2.11\pm0.21)\times10^{13}$	$(2.39\pm0.24)\times10^{38}$
Copper	$(2.48\pm0.42)\times10^{13}$	$(3.44\pm0.58)\times10^{38}$
Tungsten	$(1.97\pm0.28)\times10^{13}$	$(2.99\pm0.42)\times10^{38}$

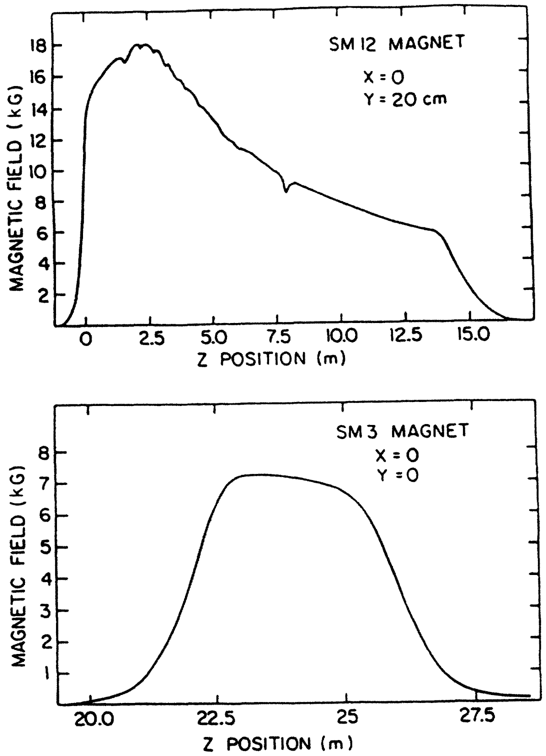

FIG. 2. The Z position dependence of the X components of the SM12 and SM3 magnetic fields.

D. Spectrometry

Knowledge of the position and angle of a particle trajectory downstream of SM12 suffices to determine the momentum vector with which the particle was produced in the target. Thus the momentum measurement afforded by the SM3 magnet is redundant and serves to distinguish particles produced in the target from particles originating elsewhere. Figure 3 shows the configuration of the four stations of wire chambers and hodoscopes which sample the particle's position along its trajectory. The track reconstruction algorithm may be simply described as matching two line segments at the SM3 bend plane and using the resulting momentum measurement (accurate to about 1%) to determine if the trajectory is consistent with originating in the target. Finally, a global fit constrained to the center of the target is used to obtain the best resolution.

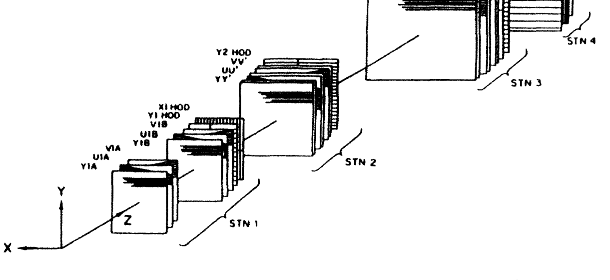

FIG. 3. The configuration of wire chambers and hodoscopes in the magnetic spectrometer.

Station 1, located between the two analyzing magnets, consisted of six planes of multiwire proportional chambers and two planes of scintillation hodoscopes. The proportional chambers were of 2 mm sense wire spacing, yielding a spatial resolution of 600 μm (rms). They operated at 90—95% efficiency due to dead-time limitations. The two planes of hodoscopes measured the X and Y positions of the trajectory with scintillator paddles about 10 cm wide. (See Table III for the dimensions of all scintillation hodoscopes.) All the hodoscope counters were less than 1.5 m long and had clip lines installed on the signal cables at the phototube end, enabling their time resolution to be less than the time between beam bunches.

Stations 2 and 3 each included six planes of drift chambers with 200 μm (rms) resolution. Table IV lists the dimensions for all wire chambers. The station 2 chambers were 90—95% efficient, while those in station 3 were 85—90% efficient. These efficiencies were limited by high background singles rates. The singles rate in station 3 was about twice that in station 2, due to low-energy backgrounds resulting from electromagnetic showers initiated in the Cherenkov mirrors located 1 m upstream of station 3. Stations 2 had a single plane of scintillation hodoscopes measuring the Y coordinate with paddles about 10 cm wide. Station 3 measured the X and Y coordinates with two planes of hodoscope counters which were about 20 cm wide.

Each of the three sets of wire chambers in the first three stations included three pairs of chambers, each pair measuring the Y, U, or V coordinate. The U and V coordinates differed from the Y coordinate by a small angle θ_s such that $\tan\theta_s = \pm\frac{1}{4}$. The resulting algebraic relationship between the three measured coordinates for normally incident particles provided useful discrimination in the track reconstruction algorithm. The paired planes of drift chambers were offset by half a cell with respect to each other, with the result that for normally incident particles the sum of the drift times from the paired planes was a constant. It was thus possible to efficiently reject pairs of hits produced in interactions from neighboring beam bunches.

Finally, station 4 consisted of a plane of 20-cm-wide hodoscope counters measuring the Y coordinate and two planes of proportional tubes with 2.5-cm-wide cells measuring the X and Y coordinates. This station was located behind the calorimeter, three absorption lengths of concrete, and nine absorption lengths of zinc. It served to identify muons.

E. Acceptance

The geometrical arrangement of the spectrometer elements which serve to measure the particle trajectories and the location of absorber in the SM12 magnet determine the acceptance of the apparatus. A simple means for specifying the single hadron geometrical acceptance for

TABLE III. Parameters of the scintillation-hodoscope planes.

	$Y1$	$X1$	$Y2$	$X3$	$Y3$	$Y4$
Z position (m)	21.01	21.04	28.32	46.66	46.92	51.87
Horizontal aperture (cm)	121.9	121.9	162.6	264.2	264.2	294.6
Vertical aperture (cm)	152.4	152.4	172.7	233.7	233.7	254.0
Segmentation (horizontal × vertical)	2×12	12×2	2×17	13×2	2×13	2×14
Counter elements						
Width (cm)	12.7	10.2	10.2	22.5 (11.0)[a]	17.8 (19.1)[a]	17.8 (20.3)[a]
Length (cm)	61.0	76.2	81.3	116.8	132.1	147.3
Thickness (mm)	4.76	4.76	3.72	6.35	6.35	6.35

[a] Edge counters.

the spectrometer is to consider a projection of the apparatus' coordinate system onto the Y-Z plane. For any point (Y_0,Z_0) in this projection a linear relationship is established between the Y and Z components of the momenta (p_Y and p_Z) of those trajectories which pass through that point:

$$p_Y=\left[\frac{Y_0-Y_T}{Z_0-Z_T}-\theta_Y^{\text{beam}}\right]p_Z+\frac{\Pi(Z_0)}{Z_0-Z_T}\ ,$$

where

$$\Pi(Z_0)=\frac{q}{c}\int_{Z_T}^{Z_0}dz'\int_{Z_T}^{z'}dz''B_X(z'')$$

and where Y_T and Z_T are the Y and Z positions of the target, θ_Y^{beam} is the angle of the beam with respect to the spectrometer axis in the Y-Z plane, $B_X(z)$ is the X component of the magnetic field along the trajectory, and q is the charge of the particle for which the trajectory is considered. The geometrical acceptance is defined by the most stringent of the aperture restrictions. Since the angular acceptance in X is limited to $-0.041<\theta_X<0.019$ rad, the quantity $(p_T-p_Y)/p_Y$ does not exceed 20% anywhere within the acceptance. Figure 4 shows the area of geometrical acceptance in the laboratory frame and transformed to the proton-nucleon center-of-momentum frame. The five aperture points indicated by straight lines in Fig. 4 are the upstream end of the beam dump, the top and bottom of station 3, and the upper and lower aperture limits at the exit of the SM12 magnet.

F. Resolution

A principal goal of the first data run was to take advantage of the excellent measurement resolution afforded by the open aperture and the high-transverse-momentum

TABLE IV. Parameters of the wire chambers.

		Z (m)	Aperture X (cm)	Y (cm)	Wire spacing (mm)	Number of wires
Station 1	$Y1A$	18.91	128.3	149.6	2.0	736
	$U1A$	19.17	128.3	152.4	1.94	896
(Proportional	$V1A$	19.42	128.3	152.4	1.94	896
wire	$Y1B$	20.11	128.3	149.6	2.0	736
chambers)	$U1B$	20.36	128.3	152.4	1.94	896
	$V1B$	20.62	128.3	152.4	1.96	896
Station 2	YY'	27.55	167.6	178.8	10.0	176
(Drift	UU'	27.80	167.6	182.9	9.7	208
chambers)	VV'	28.06	167.6	182.9	9.7	208
Station 3	YY'	45.79	269.2	233.3	20.0	112
(Drift	UU'	46.04	269.2	242.6	19.4	144
chambers)	VV'	46.30	269.2	242.6	19.4	144
Station 4	PTX	54.81	365.8	315.0	25.4	144
(Proportional tubes)	PTY	55.85	363.2	375.9	25.4	142

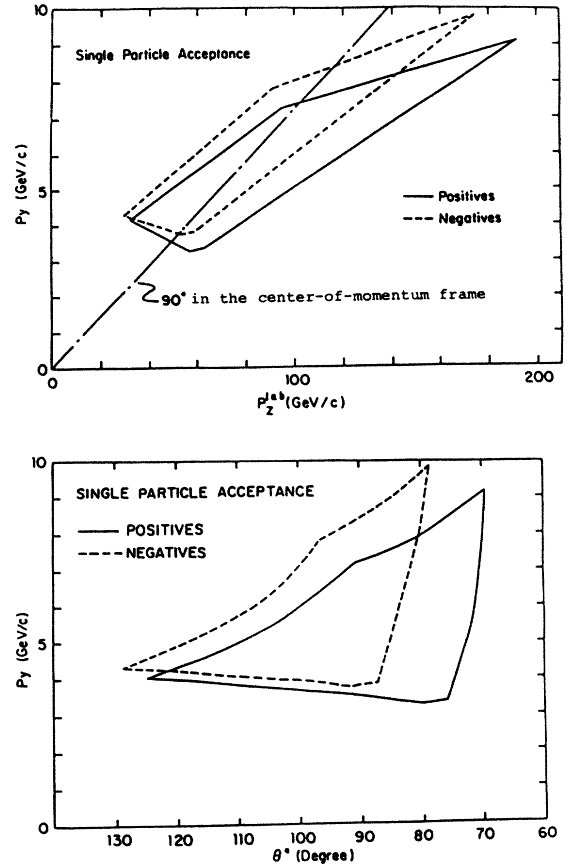

FIG. 4. The kinematic region of acceptance in the laboratory and center-of-momentum frames. In the laboratory frame each aperture point is represented by a straight line. The five aperture points shown are the upstream end of the beam dump, the top and bottom of the station 3 detection planes, and the upper and lower aperture limits at the exit of the SM12 magnet.

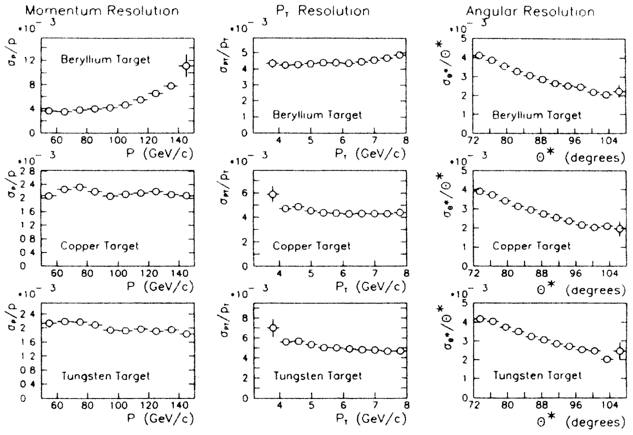

FIG. 6. Estimates of the measurement resolution in momentum, transverse momentum, and production angle for the three targets. The estimates are obtained using Monte Carlo techniques and the vertical error bars are statistical.

kicks of the analyzing magnets. In order to reduce the effects of multiple scattering, the SM12 magnet is filled with helium, and a helium bag was placed between the exit of the SM12 magnet and station 1, as well as inside the SM3 magnet aperture. Figure 5 indicates the contributions of wire-chamber spatial resolution, multiple scattering in the target of the final state hadron, and target length to the resolution in the measurement of momentum. Monte Carlo studies indicated that the beam divergence was also a significant contribution to the resolution in transverse momentum and production angle. For example, effects of the beam divergence raised the uncertainty in the measurement of production angle in the tungsten target from 0.2% to 0.3% at 90°. Figure 6 shows the results of Monte Carlo resolution studies. It should be noticed that the measurements of momentum, transverse momentum, and production angle are highly correlated. Thus, even though the momentum resolution for the beryllium target was significantly worse due to effects of the target length, the measurement resolution in transverse momentum and production angle was similar for all three targets.

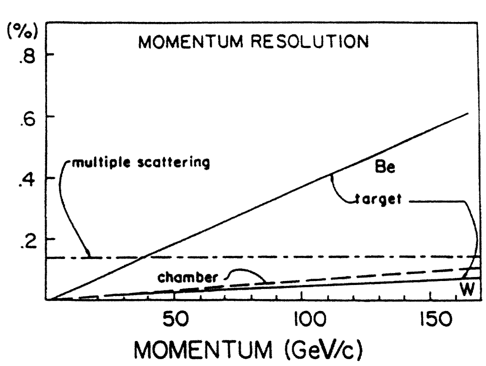

FIG. 5. Contributions to the momentum measurement resolution.

Though good measurement resolution is more useful for studying kinematically localized phenomena such as resonances than for studying the shapes of cross sections, it is also valuable in measuring the slopes of steeply falling distributions. In the case of the strong p_T dependence of single hadron production our bin size is bounded below by the requirement that the statistical errors be near 10%. The resulting 200-MeV/c bin size is about 10σ wide and the contamination in any raw data bin due to resolution smearing is less than half a percent.

G. Transverse-momentum scale determination

NMR probes placed in the SM12 and SM3 magnets during the course of the data run indicated that the magnitudes of the magnetic fields were stable to better than one part in 10^4. Using lepton-pair events in the mass region of the upsilon resonances, we have estimated the uncertainty in our transverse-momentum scale to be 0.3%.

H. Calorimetry

The calorimetry served two functions: (1) a minimum energy deposited in the calorimeter was one of the trigger requirements for the hadron and electron triggers, and (2) characteristics of the shower development allowed the off-line analysis to distinguish electrons from hadrons. The calorimeter, situated between stations 3 and 4, was longitudinally segmented into two sections: an electromagnetic part and a hadronic part. Both were sampling calorimeters consisting of plastic scintillators and absorbers of dense material. The electromagnetic part was arranged in 32 layers of 3-mm lead and 6-mm scintillators, a total of 19 radiation lengths. The scintillators were grouped into four modules (4, 9, 9, and 10 layers from the upstream end) in the longitudinal direction. A 1.27-cm-thick lead sheet was placed in front of the calorimeter between the two planes of hodoscope counters in station 3. This lead sheet and the thin first module (two radiation lengths) were designed to provide good electron/hadron identification based on prototype test results.[12] In the horizontal and vertical dimensions the calorimeter measured 2.9×2.4 m^2. Each module was divided in half in the horizontal direction and into 12 segments in the vertical direction. The light output of each segment was collected by a six-stage phototube through an acrylic light guide.

The hadronic part of the calorimeter consisted of two modules in the longitudinal direction. The first module consisted of 12 layers of 2.5-cm-thick iron sheets and 6-mm-thick scintillator paddles. The second module consisted of 20 layers of 5-cm-thick iron sheets and 6-mm-thick scintillator paddles. The total thickness amounted to nine absorption lengths including the electromagnetic part, which was one absorption length thick. These two modules measured 3.1×2.6 m^2 in cross section. The transverse segmentation of the two hadronic modules was similar to that of the electromagnetic part, but with 13 segments in the vertical direction. The light output of each segment was collected on a wavelength shifter bar and transmitted to a phototube through an acrylic light guide. The attenuation of the light along the wavelength shifter bar was corrected by masking the surface of the wavelength shifter with an aluminized Mylar sheet. The entire calorimeter was temperature stabilized inside a vinyl hut. Figure 7 shows the structural design of the calorimeter.

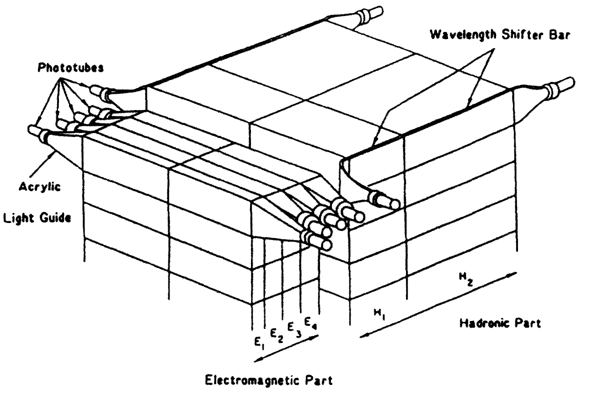

FIG. 7. The structural design of the calorimeter.

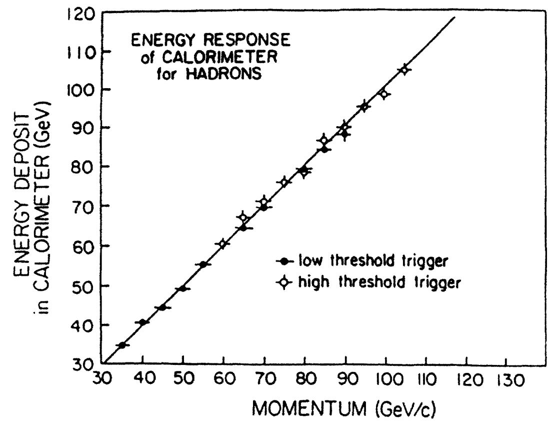

FIG. 8. The linearity of the calorimeter response.

The signals from the dynodes of all the phototubes of the calorimeter were summed with an array of linear summing circuits. The sum was used for the fast triggers. The signal from each phototube anode served as input to an 8-bit analog-to-digital converter with a quadratic response and 4 μs conversion time.

Calibration of the phototube gains was accomplished using the independent momentum measurement afforded by the SM3 magnet and the tracking chambers. Figure 8 exhibits the linearity of the calorimeter response. An energy resolution for hadron showers of $\sigma_E/E=0.75/\sqrt{E}$ (where the energy E is expressed in units of GeV) was achieved.

I. Hadron identification

Pions, kaons, and protons were distinguished by a ring-imaging Cherenkov detector. The radiator vessel, situated between stations 2 and 3, measured $3\times3\times15$ m^3 and was filled with helium at a pressure slightly higher than atmospheric. Mirrors installed at the downstream end of the radiator vessel reflected the Cherenkov photons back upstream to a multistep avalanche chamber sensitive to ultraviolet photons. During the test run, only one of two photon detectors was available; hence, only half the aperture was instrumented with mirrors. Furthermore, fast analog-to-digital converters for this detector had not yet been installed, so CAMAC analog-to-digital converters were used, with the result that the readout time for events with Cherenkov identification information was longer than that for events without the Cherenkov information by a factor of 50. In order to keep the total readout dead time under 15%, less than 10% of the events written to tape contained Cherenkov information. Details of the performance of the Cherenkov detector are presented in Ref. 13, and measurements of the atomic-weight dependence in the production of identified hadrons have been published in Ref. 14. For the purposes of the work presented here we have used the larger data sample of unidentified hadrons.

III. THE DATA ACQUISITION

A. Triggering

Readout for single hadron events was triggered on two conditions. The first derived from the five banks of hodoscope counters. A hardware look-up table operating at 100 MHz received the discriminated, synchronized hodoscope signals as inputs.[15] Preloaded with combinations of counters corresponding to a particle produced in the target and traversing the open apertures of the SM12 and SM3 magnets, this "trigger matrix" generated information indicating whether allowed combinations of counters fired. The rate capability of this device allowed the trigger to distinguish individual beam bunches of incident beam particles in the accelerator's 53-MHz rf structure.

The second requirement in the fast hadron trigger was discrimination on the total energy deposited in the calorimeter. This requirement was used to reduce the trigger rate to a level acceptable for recording on magnetic tapes. Figure 9 indicates the hadron trigger efficiency folded into the acceptance, comparing it to the geometrical acceptance alone.

B. Event readout and storage

The data from 8000 channels of time-to-digital converters, analog-to-digital converters, and latches were transferred at the rate of 200 ns per 16-bit word to a buffer of one megabyte capacity during the one-second beam spill. A Unibus link to a PDP-11/45 allowed these events to be recorded on magnetic tapes during the nine seconds between spills. On the average half a megabyte of data was stored per spill, the most likely event length being 250 16-bit words. Ten million events were recorded during four days, with a readout dead time of less than 15%. This data acquisition system is described in detail in Ref. 16.

IV. THE DATA ANALYSIS

A. The Monte Carlo technique

A goal of the off-line physics analysis was to emulate the apparatus comprehensively in software and generate simulated raw data using Monte Carlo calculational techniques. The CERN-supported apparatus-simulation software package GEANT (Ref. 17) was employed to this end. Further routines were written to reproduce the raw data format sent to magnetic tape by the data-acquisition system. Thus the tapes generated via the Monte Carlo technique could be subjected to the same analysis routines as the raw data tapes. This method allowed diagnostic investigation of all the analysis routines, even at the level of the raw data unpacking algorithms. Input parameters to the apparatus simulation, such as wire-chamber and hodoscope counter efficiencies, the spatial resolution of the wire chambers, and the energy resolution of the calorimeter, were "measured" by analyzing the emulations of the

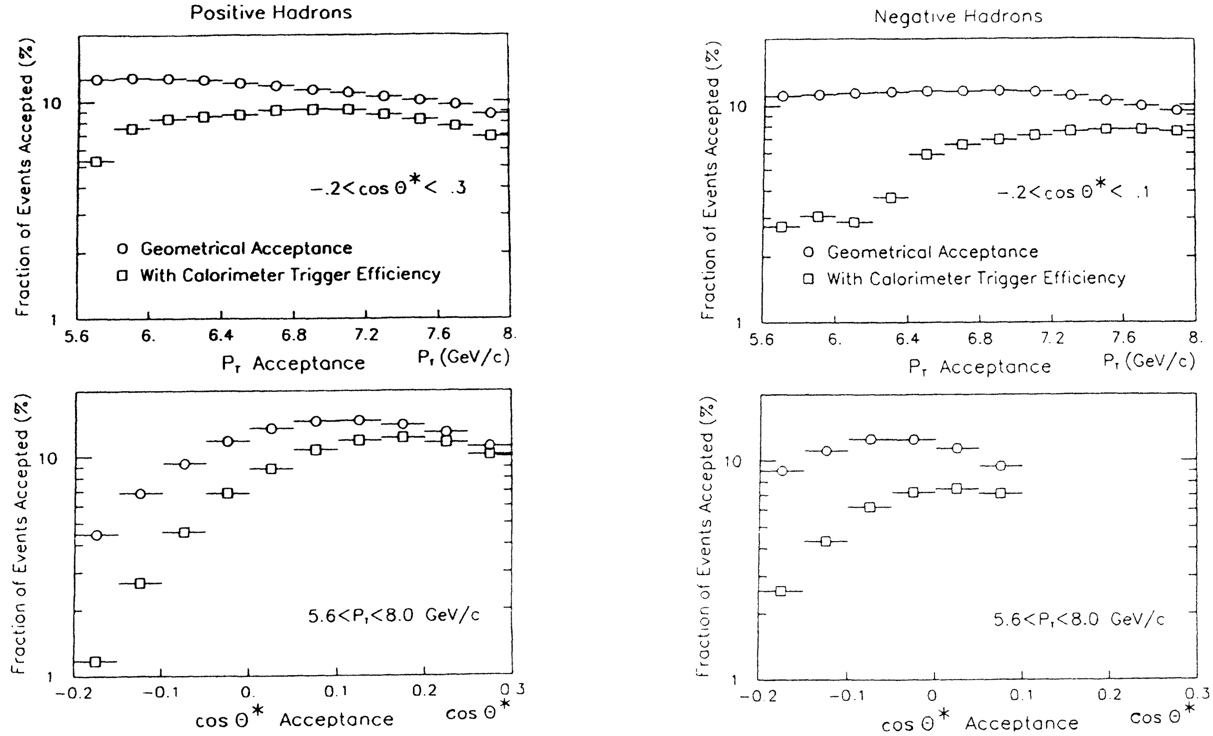

FIG. 9. The fraction of events accepted as a function of transverse momentum and production angle for positive and negative hadrons produced in the beryllium target. The effect of the calorimeter trigger efficiency is indicated. We assumed that the production of hadrons is independent of the azimuthal angle ϕ. Since for both positive and negative hadrons the geometrical acceptance was limited to 20% of 2π, the fraction of events accepted does not exceed 20%.

raw data tapes using routines identical to those which measured these parameters on the raw data tapes themselves. An iterative procedure was then employed to readjust the input parameters until the analysis of the emulations yielded the same results as analysis of the raw data tapes. Calibration triggers were also simulated by the Monte Carlo routines. For example, prescaled hadron triggers with energy deposition thresholds lower than those in the single hadron triggers analyzed for cross section measurements were used to measure the response curves of the higher threshold triggers. Such analysis was carried out for both the raw data calibration triggers and the emulated calibration triggers. An iterative procedure then allowed fine-tuning of the Monte Carlo simulation of the calorimeter energy-deposition requirement in the single hadron trigger.

The response of the apparatus to a variety of input physics distributions was measured via the Monte Carlo technique and the results inverted to generate cross sections from the raw data distributions. The final cross sections are those which, when used as input to the Monte Carlo program, resulted in the calculation of fit values for the cross section identical to those serving as input to within statistical errors.

B. Cuts and weights applied to the data

The means of measuring cross sections described above requires analyzing the Monte Carlo data with software cuts identical to those used in the analysis of the raw data. Such cuts are used to eliminate from the final raw data sample events which occur in kinematic regions where the efficiency of the apparatus is too low to simulate reliably, or where contamination from backgrounds may occur, such as near aperture points. Following is a descriptive list of all cuts and weights. Table V lists the cumulative number of events which passed the cuts.

1. Cuts

a. Track reconstruction. At least one track was required to have been reconstructed in the magnetic spectrometer. The tracking subroutines required at least four of the six chambers in station 1 to have fired, and at least three of the six chambers in each of stations 2 and 3.

b. Hadron identification. The track was required to point at a cluster of energy deposition in the calorimeter. The energy deposited was also required to match the SM3 magnet momentum determination to within three standard deviations of the calorimeter energy resolution. All entries in the hadron sample failed an electron identification algorithm based on the energy deposited in the electromagnetic part of the calorimeter. The positive identification efficiency for this algorithm was estimated to be 95% (Ref. 12). Hadron tracks were further required to fire no more than one of the two muon chambers in station 4.

c. SM12 geometrical-aperture cuts. The algorithm which reconstructed the particle trajectory through the SM12 aperture used the momentum as measured by the SM3 magnet to roughly determine the particle position at the Z coordinate of the target. A loose cut on the target position was applied. The trajectory was then constrained to originate in the center of the target and a new trajectory (and another momentum) was determined. Aperture cuts were made on the Y position of the trajectory at the most stringent aperture points. The cuts were made 2σ more stringent than the surveyed position of the absorber, where σ is the spatial resolution of the traceback algorithm at the Z position of the aperture point. The analysis was repeated with 5σ cuts to ascertain that these cuts affected the final determination of the cross sections only at the level of about 1%.

d. X-angle limits. The angle of any particle trajectory in the X-Y plane was subject to the requirement

TABLE V. Number of events passing off-line analysis cuts.

	Positive hadrons			Negative hadrons		
	Be	Cu	W	Be	Cu	W
Track reconstruction	112 833	190 955	192 279	13 776	17 519	16 709
Hadron identification	108 273	187 473	188 753	11 518	16 297	15 598
Traceback apertures	62 201	120 274	122 930	4 020	7 339	7 509
Hodoscope matrix requirement	57 665	113 620	116 104	3 634	6 738	6 925
X-angle cut	49 354	97 760	99 673	3 056	5 656	5 770
Hodoscope apertures	46 670	92 514	94 364	2 970	5 488	5 565
Calorimeter-trigger efficiency cut	40 293	79 848	81 692	2 140	4 112	4 149
Fraction of events passing all cuts	36%	42%	42%	16%	23%	25%
Number of events in the kinematic range of the cross sections shown	2 678	4 930	5 018	342	664	675

$3 < |\theta_X| < 26$ mrad, where θ_X was measured with respect to the spectrometer axis. This cut excluded regions of uncertain efficiency due to the construction of the calorimeter, which had a vertical gap around $X = 0$ about 5 cm wide.

e. Hodoscope-aperture requirement. Particle trajectories which passed within 5 cm of any edge of the five hodoscope banks upstream of the calorimeter were cut from the final data sample. This cut, combined with the SM12 aperture cuts and the X angle cuts, defined the geometrical acceptance of the apparatus.

f. Trigger-matrix requirement. Further cuts on individual trajectories ensured that the trajectory considered indeed satisfied the hardware trigger requirements. One such requirement was the trigger matrix, which allowed only specific combinations of the counters in three Y hodoscope banks upstream of the calorimeter. All trajectories not passing through an allowed combination of these counters were eliminated from the data sample. Also, all five hodoscope counters along the trajectory were required to have fired.

g. Calorimeter-trigger efficiency. The other hardware trigger requirement was that the energy deposited in the calorimeter exceed a specific threshold. Given the track position at the calorimeter and the energy deposited in each module of the calorimeter, one can calculate the trigger efficiency using the results of the analysis of the prescaled, lower threshold, calibration triggers. Extensive studies of various calorimeter efficiency cuts between 50 and 95% determined that systematic uncertainties in the correction for this cut were smaller than the statistical uncertainties (see Sec. IV A). For the results shown here we use a calorimeter efficiency cut of 50%.

2. *Weights*

a. Tracking efficiency. The tracking efficiency was calculated for each run using the wire-chamber efficiencies and the tracking program requirements. Corrections due to correlations in the chamber efficiencies were calculated and found to be of the order of a few percent. Each track entered into the final raw data sample was weighted by the multiplicative inverse of the tracking efficiency for the corresponding run. For the data runs included in the final data sample the tracking efficiency was at least 88% and typically around 97%.

b. Nuclear absorption in the apparatus. There were three principal contributions to the absorption of hadrons upstream of the calorimeter. These were the absorption in the target, the absorption in the Cherenkov counter mirrors (1.8% probability), and the absorption in the rest of the apparatus upstream of the Cherenkov mirrors (1.2% probability). (It was assumed that any inelastic collision in the Cherenkov mirrors results in the production of several particles at small angles, ruining the track reconstruction in the station 3 drift chambers.) The largest of these contributions was the absorption in the target. For each track an interaction vertex was generated by the Monte Carlo method using the beam parameters. Given the reconstructed production angle, an absorption probability was computed and used to weight that hadron's contribution to the data sample. The absorption probability did not exceed 15% for any hadron and the most likely value of the absorption probability was 4%.

c. Dihadron event correction. Less than 0.5% of the events in the event sample contained two hadrons. For these events, a weight was applied to each hadron. This weight was equal to the calorimeter trigger efficiency for that track divided by the calorimeter trigger efficiency for the entire event. This weight factor reconciled the raw data sample with the Monte Carlo sample, for which no two-particle events were generated.

d. Decay-in-flight correction. Kaons and pions which decayed to muons upstream of the calorimeter usually failed the calorimeter deposition trigger requirement and always failed the off-line hadron identification algorithm. It was also estimated that negligibly few of the kaons which had decayed to pions satisfied the target cut, even if the flight path of the kaon had been successfully reconstructed. Thus all hadron tracks were weighted by the inverse of a decay probability. This decay probability was a weighted sum of the decay probabilities for pions, kaons, and protons, using relative yields obtained from Ref. 1. The weights used were 0.53/0.27/0.20 for positive hadrons and 0.84/0.14/0.02 for negative hadrons. The overall decay probabilities averaged 3.2% and did not exceed 6% for any track.

C. Backgrounds

The cuts described in the previous section allowed some background events to contaminate the data sample. These background events were of two types. The first type consisted of events containing an electron or a muon which had been misidentified as a hadron by the calorimeter information. The second type of background event contained a hadron produced elsewhere than in the target. Estimates of the magnitude of the contamination were calculated in the following manner.

1. *Electron or muon misidentification*

Electrons were identified by a large energy deposit in the electromagnetic part of the calorimeter. The fraction of the hadron sample identified as electrons was under 0.3%. Since the efficiency for positive identification of the electron-finding algorithm is estimated to be 95%, the contamination of the hadron sample by electrons should be less than 0.015%.

Muons may be misidentified as hadrons if they deposit a large fraction of their energy (at least 70%) in the calorimeter. The number of tracks firing both muon chambers but passing all other hadron requirements was 0.06% of the total hadron sample. The trajectories of muons which deposit most of their energy in the calorimeter may deviate from straight lines enough to miss the muon identification window in the muon chambers in station 4. Analysis of a clean muon sample (consisting of tracks originating in the upstream end of the beam dump and traversing the concrete absorber in the SM12 magnet) revealed that the number of muons which satisfy all hadron requirements is less than half the number of muons which fire both muon chambers but pass all other hadron requirements. Since the hadron identification algorithm requires that at least one of the muon chambers not fire, we estimated the muon contamination to be under 0.03%.

2. *Track reconstruction backgrounds*

An estimate of hadrons produced in the interactions of beam protons elsewhere than in the target was obtained by analyzing runs during which the target was removed from the beam. From a total sample of 10^{12} incident protons, the rate for producing events passing all hadron analysis cuts was found to be less than 0.5% of the rate for data with the target in place. These events presumably contained hadrons produced in the target holder or in the window of the beam pipe just upstream of the target holder.

Another source of background was secondary interactions of hadrons in material downstream of the target, e.g., the beam dump, which produce hadrons passing all analysis cuts. The algorithm which traced particle trajectories through the SM12 magnetic field using the initial momentum estimate determined by the bend angle in the SM3 magnet produced a sharply peaked distribution for the Y position of the tracks at the Z position of the target center. This target Y distribution was well approximated as a Gaussian curve with a full width at half maximum (FWHM) of 1.2 cm superimposed on a low-level background. By fitting this distribution we were able to estimate the contamination from hadrons originating elsewhere than in the target. Arbitrarily using a quadratic function to fit the background shape, we were able to estimate the number of background trajectories passing the target cut requirement. We estimated the background from this source to be less than 1%.

V. RESULTS AND CONCLUSIONS

A. The P_T dependence of the single-hadron cross sections

A typical parametrization for the transverse-momentum dependence at a fixed production angle is

$$E\frac{d^3\sigma}{dp^3}=A_0p_T^{-n}(1-x_T)^b .$$

Since the measurements described in this paper were all taken at a fixed center-of-mass energy, it is impossible here to distinguish the x_T dependence from the p_T dependence. We therefore choose to fix b at values quoted in Jöstlein *et al.* ($b=7.3$ for positive hadrons and $b=10.7$ for negative hadrons) and fit the data with the above parametrization to determine A_0 and n. It should be borne in mind as one interprets the fit results that the parameters b and n are highly correlated. Thus a change in b results in a similar change in n.

Table VI shows the values of A_0 and n for the different angular regions covered for each target. Figure 10 shows the cross sections per nucleon obtained from the beryllium target data as an example. These cross sections are averaged over the cosθ^* range indicated and over the 0.2-

TABLE VI. The values of the fit parameters A_0 and n for the invariant cross sections per nucleon for positive and negative hadrons from each target. The functional form of the fit is $f(p_T)=A_0p_T^{-n}(1-x_T)^b/[p_0^{-n}(1-x_0)^b]$, where $p_0=6.15$ GeV/c and $x_0=2p_0/s$, so that A_0 is the value of the fit evaluated at 6.15 GeV/c. The parameter b is fixed at 7.3 for positive hadrons and at 10.7 for negative hadrons. The cross section is fitted over the region from 5.6 to 8.0 GeV/c in transverse momentum.

	cosθ^* bin	Beryllium			Copper			Tungsten		
		A_0 [pb/(GeV^2/c^3)]	n	χ^2/DF	A_0 [pb/(GeV^2/c^3)]	n	χ^2/DF	A_0 [pb/(GeV^2/c^3)]	n	χ^2/DF
Positive hadrons	(−0.2)–(−0.1)	6.81±0.75	6.54±1.87	6.2/6	8.29±0.68	9.10±1.35	12.0/8	8.13±0.71	11.38±1.55	15.7/9
	(−0.1)–0.0	7.70±0.48	9.54±1.02	10.9/8	9.49±0.44	8.54±0.67	17.0/10	12.46±0.55	9.73±0.66	10.4/10
	0.0–0.1	10.97±0.44	9.60±0.62	10.4/10	12.53±0.39	8.60±0.44	7.7/9	14.02±0.44	9.98±0.47	9.6/9
	0.1–0.2	11.41±0.40	10.37±0.53	19.9/10	13.44±0.36	9.99±0.39	16.7/10	15.90±0.43	10.03±0.39	10.9/10
	0.2–0.3	10.88±0.45	10.41±0.58	14.5/10	12.78±0.39	9.91±0.44	7.3/10	15.18±0.45	9.73±0.44	8.0/10
Negative hadrons	(−0.2)–(−0.1)	4.21±0.63	3.50±1.92	2.2/8	4.83±0.53	7.04±1.49	12.4/9	4.89±0.63	2.24±1.56	3.2/8
	(−0.1)–0.0	5.24±0.48	7.08±1.09	10.0/8	4.87±0.36	6.88±0.88	21.1/10	5.97±0.43	6.02±0.85	11.4/9
	0.0–0.1	3.98±0.36	6.02±1.19	10.8/8	5.54±0.33	4.41±0.74	10.5/9	6.72±0.39	6.78±0.76	10.7/10

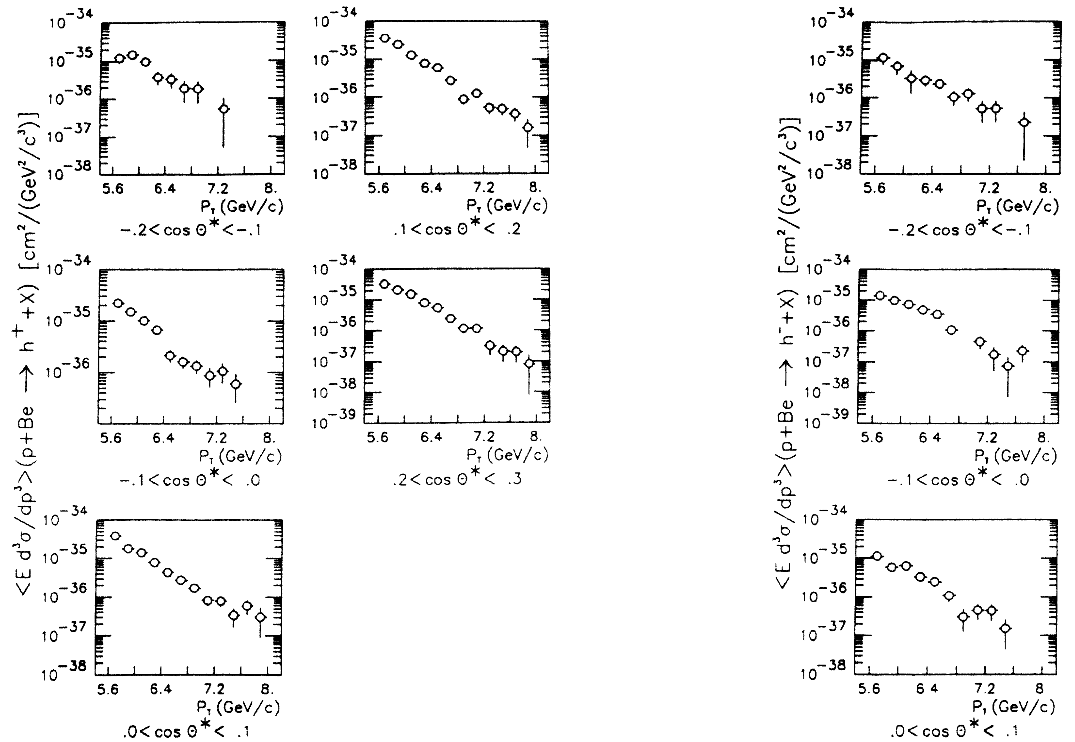

FIG. 10. The inclusive invariant cross sections per nucleon as a function of transverse momentum for positive and negative hadrons produced in the beryllium target. The cross sections are averaged over the contiguous $\cos\theta^*$ bins indicated and over the p_T bins specified by the horizontal error bars.

GeV/c p_T bins specified by the horizontal error bars. The vertical error bars indicate statistical uncertainties only. In addition, there are normalization errors of 10%, 17%, and 14% for the beryllium, copper, and tungsten cross sections, respectively.

Our data confirm the steep dependence on p_T observed previously.[1] Our values for n at $\theta^* = 90°$ agree with those measured by Jöstlein *et al.* to about one standard deviation, even though the p_T ranges of the fits ($3.3 < p_T < 5.5$ GeV/c for Jöstlein *et al.*) differ. Our purpose in studying these fits is to quantify the angular dependence of the slope of the invariant cross section versus p_T (indicated by the value of n) as well as its magnitude (indicated by the value of A_0). The fits may be considered somewhat artificial due to the fact that we cannot measure the angular dependence of the parameter b. The positive hadron data yield a slight indication that the cross section falls more steeply at more forward production angles. The dependence of A_0 on production angle shows that the cross section rises through 90° for positive hadrons and is consistent with being flat for negative hadrons. Our measurements of the cross section are about 40% lower than those quoted in Antreasyan *et al.*, independent of transverse momentum. This discrepancy might be accounted for by the normalization uncertainties (quoted as 25% by Antreasyan *et al.* and 10% here for the beryllium target data) and the transverse-momentum scale uncertainties (1% for Antreasyan *et al.* and 0.3% here.)

A standard parametrization of the atomic weight A dependence of these cross sections is

$$\frac{d^3\sigma_A}{dp^3} = A^{\alpha}\frac{d^3\sigma_0}{dp^3} ,$$

where α and $d^3\sigma_0/dp^3$ are variable parameters which depend on p_T and θ^*. For each bin a two-parameter fit to the cross sections measured for the three targets yielded a χ^2 for one degree of freedom. The data presented here confirm the power-law dependence of the cross sections on A ($\langle\chi^2\rangle = 0.77$ for positive hadrons and $\langle\chi^2\rangle = 1.0$ for negative hadrons), as well as the values of α greater than 1 determined previously.[1] Figure 11 exhibits the dependence of α on transverse momentum. The vertical error bars indicate statistical uncertainties. Because of the relative uncertainties in the normalization for the three targets, there is in addition a global uncertainty of ± 0.03 (limit of error) in these measurements of α.

B. The angular dependence of the single-hadron cross sections

We present measurements of the angular dependence of single-hadron invariant cross sections in Fig. 12 and Table VII. The cross sections shown are averaged over the p_T region from 5.6 to 8.0 GeV/c and over the contiguous $\cos\theta^*$ bins indicated by the horizontal errors bars. Here again there are additional normalization uncertainties of 10%, 17%, and 14% for the beryllium, copper, and

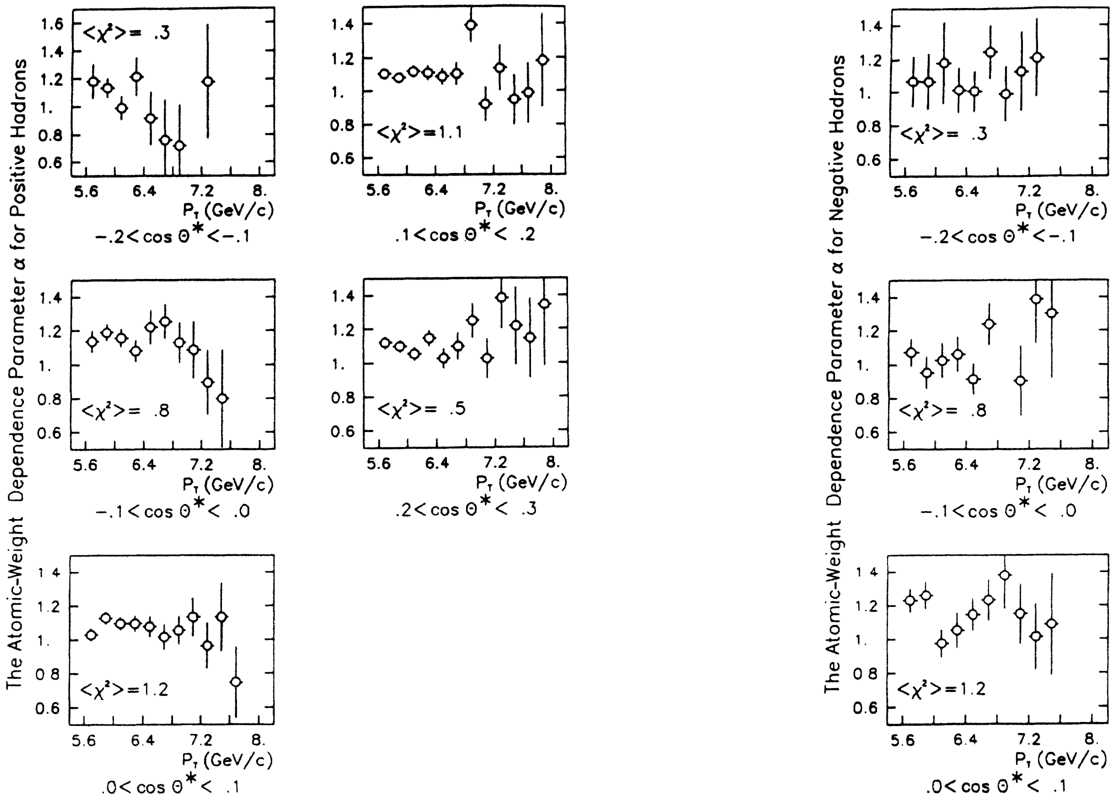

FIG. 11. The atomic-weight dependence parameter α as a function of transverse momentum for positive and negative hadrons. The bins are identical to those in Fig. 10. The vertical error bars indicate statistical uncertainties only. There is an additional global uncertainty of 0.03 units due to the relative normalization uncertainties in the data from the three nuclear targets.

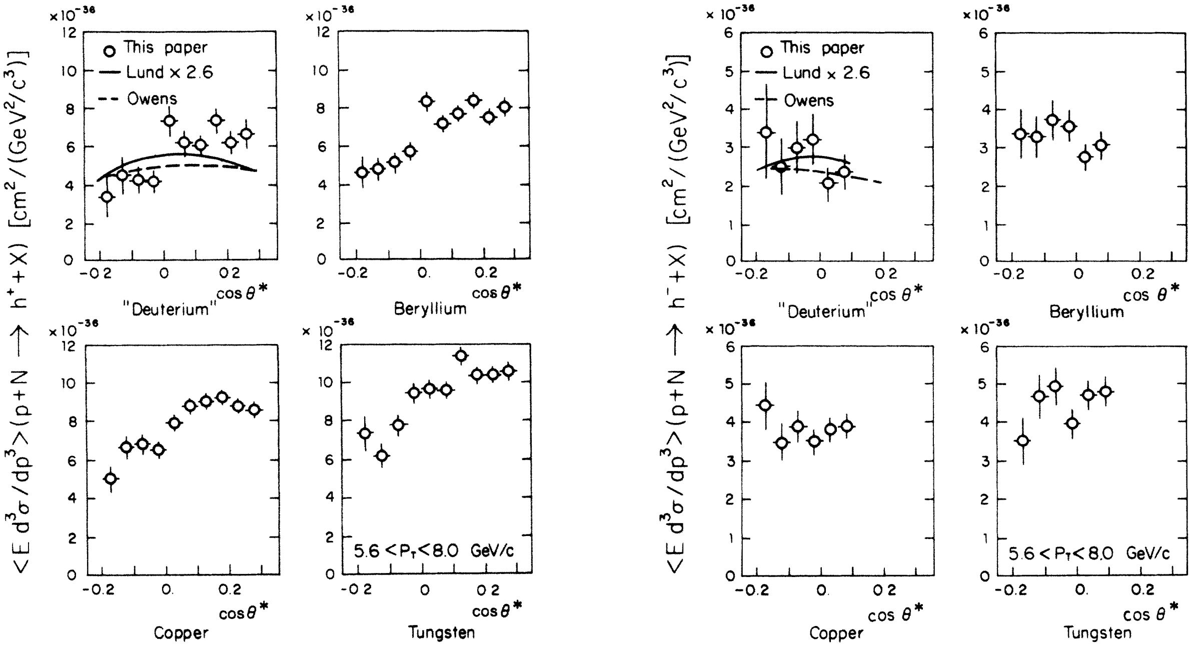

FIG. 12. The inclusive invariant cross sections per nucleon as a function of production angle for positive and negative hadrons produced in each target. The cross sections are averaged over the p_T region from 5.6 to 8.0 GeV/c and over the contiguous $\cos\theta^*$ bins indicated by the horizontal error bars. The "deuterium" cross section is obtained by extrapolating from the measurements on the three metal targets, using the assumption of a power-law dependence on the atomic weight. The Lund-model calculation shown has been multiplied by a factor of 2.6 for purposes of comparison. Also shown is the result of a leading-logarithm QCD calculation (Ref. 24).

TABLE VII. The values of the single-hadron inclusive invariant cross section per nucleon as a function of production angle for the three targets. The cross sections are averaged over the region from 5.6 to 8.0 GeV/c in transverse momentum and over contiguous $\cos\theta^*$ bins which are 0.05 units wide. The uncertainties shown are statistical only. There are also global normalization uncertainties of 10%, 17%, and 14% for the beryllium, copper, and tungsten targets, respectively.

	$\langle p_T \rangle$ (GeV/c)	$\langle \cos\theta^* \rangle$		Ed^3/dp^3 [pb/(GeV^2/c^3)]	
			Beryllium	Copper	Tungsten
Positive hadrons	5.98	−0.174	4.57±0.83	5.02±0.70	7.28±0.93
	5.98	−0.124	4.77±0.60	6.62±0.61	6.10±0.61
	5.98	−0.074	5.11±0.49	6.80±0.47	7.69±0.55
	5.98	−0.025	5.66±0.45	6.46±0.39	9.32±0.52
	5.98	0.025	8.17±0.48	7.86±0.38	9.53±0.45
	5.98	0.075	7.04±0.39	8.73±0.36	9.47±0.40
	5.98	0.125	7.52±0.38	8.97±0.34	11.26±0.43
	5.98	0.175	8.19±0.40	9.13±0.35	10.21±0.39
	5.98	0.225	7.30±0.38	8.69±0.34	10.22±0.40
	5.98	0.275	7.83±0.51	8.46±0.41	10.41±0.49
Negative hadrons	6.00	−0.175	3.31±0.65	4.43±0.64	3.46±0.61
	6.00	−0.125	3.23±0.55	3.47±0.46	4.60±0.58
	6.00	−0.075	3.66±0.49	3.88±0.40	4.87±0.49
	6.00	−0.025	3.49±0.41	3.50±0.33	3.89±0.38
	6.00	0.025	2.70±0.33	3.81±0.32	4.62±0.38
	6.00	0.075	3.01±0.36	3.88±0.32	4.71±0.38

tungsten cross sections, respectively.

We have extrapolated our measurements on the three metal targets to $A=2.01$, assuming the A^{α} parametrization. The result is shown as the "deuterium" cross section per nucleon in Fig. 12. The vertical error bars indicate the extrapolations of the statistical uncertainties. There is also a global normalization uncertainty of 13%.

In the context of QCD models, the angular dependence of the single-hadron invariant cross section arises from a convolution of scaling distributions (e.g., the x dependence of the nucleon structure functions and the z dependence of the fragmentation functions) with the angular dependencies of the constituent scattering cross sections, and with various smearing effects, such as constituent multiple scattering, initial-state interactions, etc. The relevant structure functions in the region covered by the data fall with x (Ref. 18). Therefore we can expect them to contribute to a drop in the cross section as the production angle deviates from 90° at fixed transverse momentum, since the average of x of the constituents increases as we approach the kinematic limit. Lloyd-Owen *et al.*[19] have reported that measurements at low x_T ($x_T<0.1$) in proton-proton collisions indicate that a drop of a factor of 2 becomes evident at $|\theta^*-90^\circ|\approx 70^\circ$, far outside the range of acceptance for the experiment described here. The authors, however, also show that their results are inconsistent with effects of the scaling distributions alone and must include a significant contribution from the angular dependence of the constituent subprocess. If the effects of the structure functions in this kinematic region are significant, then at higher x_T one can expect the drop to occur at angles closer to 90°, since the measurements are made in a region closer to the kinematic limit.[18,20] Indeed, our measurement of the inclusive production of positive hadrons does show such an effect, as the regular dependence is much stronger than observed by Lloyd-Owen *et al.* The effect is not so clearly evident in the negative hadron data, which cover a smaller angular range and suffer from poorer statistical precision.

The angular dependence of the inclusive h^+ cross section also exhibits an asymmetry about 90°. Two sources of asymmetry will be discussed here. First, at high x_T, where the dominant contributions are from quark-quark and quark-gluon scattering, the constituent scattering cross sections favor forward angles.[18] Furthermore, the structure function for the proton in the x region these data cover is dominated by u quarks while that for the neutron is dominated by d quarks. Since u quarks tend to fragment into positive hadrons and d quarks tend to fragment into negative hadrons, proton-neutron scattering should show an enhancement of positive hadrons in the proton direction and an enhancement of negative hadrons in the neutron direction. (Antreasyan *et al.* extracted a p-"n" cross section from their p-p and p-d data. They observed a suppression of π^+ production relative to π^- production for $x_T>0.4$ and offered as a tentative explanation that the data were taken at $\theta^*=96^\circ$, slightly backwards in the center-of-momentum frame.) The fragmentation of scattered gluons has no charge asymmetry and hence contributes weakly to these considerations. Thus in proton-nucleus interactions we may expect an enhancement of positive hadrons in the forward direction ($\theta^*<90^\circ$) and an enhancement of negative hadrons in the backward direction ($\theta^*>90^\circ$).

A quantitative estimate of these considerations may be obtained from Monte Carlo computations of constituent scattering. To this end we have employed a program based on the Lund model.[21] The standard tenets of constituent hard scattering models are used to set up the fragmentation to the final-state hadron. This fragmentation is emulated by the Lund string model, which has rather successfully described measurements of fragmentation functions obtained from electron-positron collisions.[22] We have used default values for all parameters including Eichten-Hinchliffe-Lane-Quigg (EHLQ) set No. 1 structure functions.[23] Hard constituent scattering was described by version 4.2 of the subroutine Pythia and the fragmentation process was provided by version 6.2 of the routine Jetset. The deuteron was modeled simply by summing the cross sections obtained from the emulations of proton-proton and proton-neutron interactions. The aforementioned qualitative trends may be seen in shapes of Lund-model cross sections, but we are required to scale them up by a factor of 2.6 to obtain the comparison shown in Fig. 12. Furthermore, the Lund model predicts an angular dependence for positive hadrons less steep than observed, as did Field's calculation for π^- production in $\pi^- p$ interactions in a similar kinematic region.[18] We cannot, however, exclude the possibility that residual effects of nuclear binding in our extrapolation to a deuteron cross section may yield disagreement with the Lund model.

Also shown in Fig. 12 are the results of a QCD calculation to leading-logarithm order by Owens.[24] His predictions of positive and negative hadron production at $p_T = 6$ GeV/c from 400-GeV/c proton-deuteron interactions are absolutely normalized and agree well with the measured cross section, though again the predicted angular distribution is less steep than observed.

Another source of asymmetry may arise from atomic-weight-dependent effects. An example is the effect discovered in deeply inelastic muon-nucleus scattering and described in the Introduction.[6,7] Since quarks in nuclei appear to carry smaller fractions of the nucleon momentum than quarks in a free nucleon, the constituent center-of-momentum frame appears to be moving in the beam direction as observed in the nucleon center-of-momentum frame (which is the frame in which we calculate the production angle.) Thus the production of all particles should be biased toward production angles smaller than 90°. The magnitude of the effect is comparable to the statistical precision of these data ($\approx 10\%$), however, and hence we can expect only a marginal measurement of the effect. Its principal identifying characteristic would be an enhancement with atomic weight, that is, α rising at forward angles. Figure 13 shows the dependence of α on production angle. While the data are consistent with such an effect, the statistical precision is such as to preclude an unambiguous confirmation. Clearly the average value of α of about 1.15 is due to effects consistent with multiple scattering models in the p_T region considered. An angular asymmetry in a multiple scattering model would result in an altered interpretation of the angular dependence of α. However, presumably due to the dearth of measurements of angular dependencies in hadron production at high transverse momenta, the literature on multiple scattering models includes no discussion of angular dependencies.

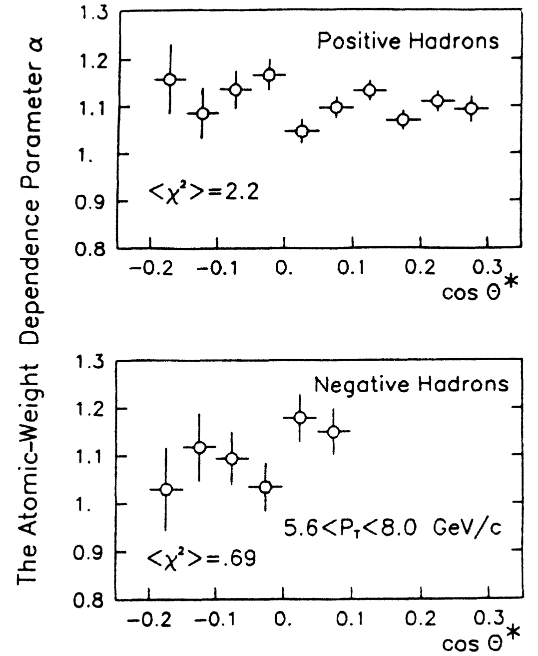

FIG. 13. The atomic-weight dependence parameter α as a function of production angle for positive and negative hadrons. The bins are identical to those in Fig. 12. The vertical error bars indicate statistical uncertainties only. There is an additional global uncertainty of 0.03 units due to relative normalization uncertainties in the data from the three nuclear targets.

Isospin invariance provides us with a simple, reliable prediction concerning the angular dependence of the sum of π^+ and π^- inclusive production cross sections. In proton-neutron interactions, the number of π^+'s produced

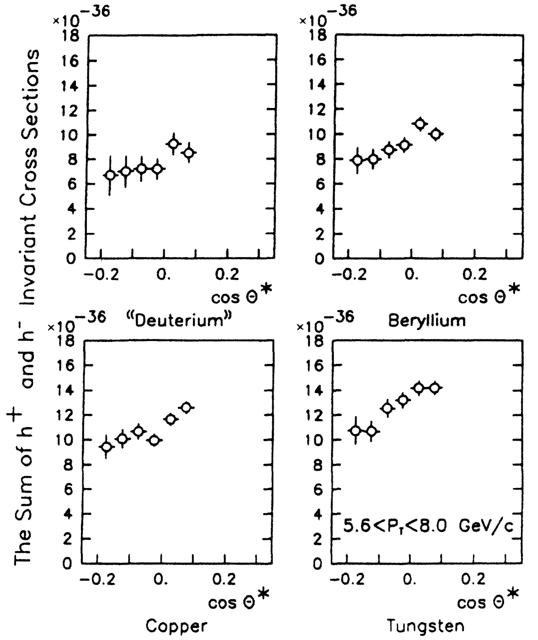

FIG. 14. The sums of positive and negative hadron inclusive invariant cross sections as a function of production angle. The "deuterium" cross section is obtained by extrapolation.

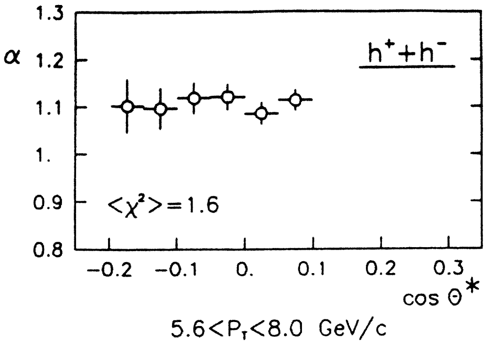

FIG. 15. The atomic-weight dependence parameter α as a function of production angle for the sums of positive and negative hadron cross sections. The bins are identical to those in Fig. 14. The vertical error bars indicate statistical uncertainties only. There is an additional global uncertainty of 0.03 units due to relative normalization uncertainties in the data from the three nuclear targets.

at an angle θ must equal the number of π^-'s produced at an angle $90° - \theta$. Since proton-proton interactions yield no angular asymmetries, we may conclude that for protons incident on an unbound assemblage of protons and neutrons, the sum of the resulting π^+ and π^- production cross sections is symmetric about 90°. Asymmetries may be interpreted as arising from nuclear effects.

In our case of unidentified hadrons we may expect an additional forward bias due to the larger admixture of K^+ and p in the positive hadron sample ($\sim$47%) than K^- and $\bar{p}$ in the negative hadron sample ($\sim$16%). Figure 14 shows the sums of the h^+ and h^- production cross sections for each target. A slight forward bias is indeed indicated; however, there is no atomic-weight dependence observed (see Fig. 15). Once again, we have used the assumption of a power-law dependence on the atomic weight to present a "deuterium" cross section. Since the softening of constituent structure functions in nuclei previously observed would bias the production of all particles toward forward angles independent of their charge, we conclude that the magnitude of such an effect is not detectable in the sum of h^+ and h^- cross sections at our level of precision. However, the apparent manifestation of the effect in the production of negative hadrons, which are 84% pions, leaves open the possibility of detecting it in the sum of π^+ and π^- production cross sections.

C. Summary of conclusions

In this section a number of physical processes have been described and our measurements compared to the expected manifestations of these processes. In the interest of clarity, let us briefly summarize them.

(1) The dependence of the inclusive hadronic production cross section on transverse momentum. Our measurements corroborate the earlier observations of a steep dependence ($\sim p_T^{-8}$) of the cross section and extend the region investigated to transverse momenta of 8 GeV/c. There is an indication that the dependence on p_T steepens at more forward production angles.

(2) The dependence of the inclusive hadronic production cross section on production angle. A comparison of our results with measurements[19] at lower x_T indicate that effects due to the proximity of the kinematic limit are appreciable. The difference in the relative shapes of the positive and negative hadron dependencies reflect the presence of neutrons in the target materials, showing that the quark flavor flow in the fundamental constituent scattering is observed. The production of positive hadrons is biased forward, as expected from simple QCD considerations. The production of negative hadrons is measured to be consistent with no angular dependence in the region covered by our data.

(3) The atomic weight dependence of the inclusive hadronic production cross section. The primary observation is the measurement of $\alpha \approx 1.15$ fairly independent of transverse momentum in the kinematic region covered by the data. This result is qualitatively consistent with constituent multiple scattering models, but better measurements and more detailed models are needed before a quantitative understanding of the process can be achieved. Measurements of the variation of the atomic-weight dependence with production angle are consistent with no angular dependence in the inclusive production of positive hadrons, but show evidence that a forward bias is present in the production of negative hadrons in nuclei of high atomic weight.

ACKNOWLEDGMENTS

We would like to extend our gratitude to the support staffs of our collaborating institutions, whose ingenuity and technical expertise provided essential contributions to this work. Special thanks are in order to the mechanical group of the Meson Department at Fermilab for their component execution of the design, construction, and assembly of the large components of our apparatus. Several of the authors gratefully acknowledge the support and encouragement they have received from the Fermilab Physics Department. This research was supported in part by the National Science Foundation, the Department of Energy, le Commissariat a l'Energie Atomique, and the U.S.-Japan Agreement in High Energy Physics.

(a)Present address: Centre d'Etudes Nucléaires de Saclay, Gif-sur-Yvette, France.

(b)Present address: Fermi National Accelerator Laboratory, Batavia, IL 60510.

(c)Present address: Florida State University, Tallahassee, FL 32306.

(d)Present address: CERN, Geneva, Switzerland.

(e)Present address: University of Helsinki, SF-00170 Helsinki-17, Finland.

(f)Present address: Columbia University, New York, NY 10027.

(g)Present address: Argonne National Laboratory, Argonne, IL 60439.

[h]Present address: University of Rochester, Rochester, NY 14627.

[i]Present address: KEK, Ibaraki-ken, 305 Japan.

[j]Present address: University of Illinois at Chicago, Chicago, IL 60680.

[k]Present address: Aerospace Corporation, 2350 East El Segundo Blvd., El Segundo, CA 90245.

[1] D. Antreasyan *et al.*, Phys. Rev. D **19**, 764 (1979); H. Jöstlein *et al.*, *ibid.* **20**, 53 (1979).

[2] R. P. Feynman, R. D. Field, and G. C. Fox, Phys. Rev. D **18**, 3320 (1978).

[3] A. G. Clark *et al.*, Phys. Lett. **74B**, 267 (1978); A. L. S. Angelis *et al.*, *ibid.* **79B**, 505 (1978); C. Kourkoumelis *et al.*, *ibid.* **84B**, 271 (1979).

[4] M. J. Longo, Nucl. Phys. **B134**, 82 (1978); A. Kryzwicki *et al.*, Phys. Lett. **85B**, 407 (1979); M. Lev and B. Petersson, Z. Phys. C **21**, 155 (1983).

[5] A. Arvidson *et al.*, Nucl. Phys. **B246**, 381 (1984).

[6] J. J. Aubert *et al.*, Phys. Lett. **123B**, 275 (1983).

[7] A. Bodek *et al.*, Phys. Rev. Lett. **50**, 1431 (1983); **51**, 534 (1983).

[8] R. L. Jaffe, Phys. Rev. Lett. **50**, 228 (1983); H. Faissner and B. R. Kim, Phys. Lett. **130B**, 321 (1983).

[9] E. L. Berger, Argonne Report No. ANL-HEP-CP-85-70, 1985 (unpublished); S. V. Akulinichev *et al.*, Phys. Rev. Lett. **55**, 2239 (1985).

[10] T. Ochiai *et al.*, Rikkyo University Report No. RUP-85-4, 1985 (unpublished).

[11] Particle Data Group, Report No. LBL-91, 1985 (unpublished).

[12] Y. Sakai *et al.*, IEEE Trans. Nucl. Sci. **NS-28**, 528 (1981).

[13] H. D. Glass *et al.*, IEEE Trans. Nucl. Sci. **NS-30**, 30 (1983); M. Adams *et al.*, Nucl. Instrum. Methods **217**, 237 (1983).

[14] Y. B. Hsiung *et al.*, Phys. Rev. Lett. **55**, 457 (1985).

[15] R. Gray and J. P. Rutherfoord, Nucl. Instrum. Methods (to be published).

[16] J. A. Crittenden *et al.*, IEEE Trans. Nucl. Sci. **NS-31**, 1028 (1984).

[17] R. Brun *et al.*, CERN Report No. DD/US/86, revised, 1982 (unpublished).

[18] R. D. Field, Phys. Rev. D **27**, 546 (1983).

[19] D. Lloyd-Owen *et al.*, Phys. Rev. Lett. **45**, 89 (1980).

[20] H. J. Frisch *et al.*, Phys. Rev. D **27**, 1001 (1983).

[21] T. Sjostrand (private communication); Comput. Phys. Commun. **27**, 243 (1982).

[22] D. H. Saxon, Rutherford Appleton Laboratory Report No. RAL-85-077, 1985 (unpublished).

[23] E. Eichten, I. Hinchcliffe, K. Lane, and C. Quigg, Rev. Mod. Phys. **56**, 579 (1984).

[24] J. F. Owens, Florida State University (private communication); see also D. W. Duke and J. F. Owens, Phys. Rev. D **30**, 49 (1984).